

## Supporting Information

# Abnormal Hypsochromic Shifts of Surface Plasmon Scattering by Atomic Ordering in Gold-Copper Intermetallic Nanoparticles

*Hyuncheol Oh,<sup>†</sup> Minjun Kim,<sup>†</sup> Youngchan Park,<sup>†</sup> Seol Ryu,<sup>\*,‡</sup> and Hyunjoon Song<sup>\*,†</sup>*

<sup>†</sup>Department of Chemistry, Korea Advanced Institute of Science and Technology, Daejeon 34141, Korea

<sup>‡</sup>Department of Chemistry, Chosun University, Gwangju 61452, Korea

\* To whom correspondence should be addressed. E-mail: sryu@chosun.ac.kr, hsong@kaist.ac.kr

## 1. Detailed Experimental Procedure

**Chemicals.** Gold(III) chloride hydrate ( $\text{HAuCl}_4 \cdot 3.6\text{H}_2\text{O}$ ,  $\geq 99\%$ , Aldrich), trisodium citrate dihydrate (SC,  $\geq 99\%$ , Aldrich), potassium carbonate ( $\text{K}_2\text{CO}_3$ ,  $\geq 99\%$ , Aldrich), and tannic acid (TA, ACS reagent), poly(vinylpyrrolidone) (PVP,  $M_w = 55,000$ , Aldrich) was used as received. Millipore-filtered water ( $18.2\text{ M}\Omega$ ) was used for all procedures.

**Preparation of 3.5 nm Au Seeds.** To synthesize the 3.5 nm Au seeds, 150 mL of the freshly prepared reducing solution of 2.2 mM SC containing 0.1 mL of 2.5 mM TA and 1 mL of 150 mM  $\text{K}_2\text{CO}_3$  was heated to  $70\text{ }^\circ\text{C}$  in a 250 mL three-necked round-bottom flask under vigorous stirring. Then, 1 mL of 25 mM  $\text{HAuCl}_4$  was rapidly injected. The solution was kept at  $70\text{ }^\circ\text{C}$  for 5 min to ensure a complete reaction of the gold precursor.<sup>1</sup>

**Seeded Growth for 20 nm Au nanoparticles.** Immediately after the synthesis of Au seeds, the sample was diluted by extracting 55 mL and adding 55 mL of 2.2 mM SC. When the temperature reached again at  $70\text{ }^\circ\text{C}$ , two injections of 0.5 mL of 25 mM  $\text{HAuCl}_4$  were done on a time interval of 10 min. This growing step comprising sample dilution and two injections of  $\text{HAuCl}_4$  was repeated until the particles reached 20 nm.<sup>1</sup>

**Characterization.** The nanoparticles were characterized by transmission electron microscopy (TEM, Philips F20 Tecnai operated at 200 kV, KAIST). X-ray diffraction (XRD) patterns were recorded on a Rigaku D/max-2500 diffractometer with a Cu  $K\alpha$  source ( $\lambda(\text{Cu } K\alpha) = 1.54\text{ \AA}$ ). The UV-visible absorption spectra were collected using a Shimadzu UV- S6 3600 spectrophotometer with a 1-cm quartz cuvette at ambient temperature.

**Ligand Exchange.** To exchange citrate with PVP, 195 mg PVP dissolved in 10 mL water were added to 40 mL of 20 nm Au colloids. It gives a total reaction volume of 50 mL and PVP concentrations of  $3.9\text{ mg mL}^{-1}$ . The mixture was stirred for 12 h at room temperature. The PVP-

functionalized nanoparticles were centrifuged at 10,000 rpm for 30 min and redispersed in ethanol.<sup>2</sup>

**Preparation of Thin-Film by Evaporative Self-Assembly.** Polished silicon wafers with a 2.2 nm native oxide were cleaved into  $10 \times 10 \text{ mm}^2$  pieces. These substrates are cleaned by sonication in methanol for 20 min. A high surface affinity for the nanoparticles was achieved by derivatization of the silicon substrates in a Piranha solution (a mixture of sulfuric acid ( $\text{H}_2\text{SO}_4$ ) and hydrogen peroxide ( $\text{H}_2\text{O}_2$ )) for 60 min, followed by thorough rinsing in methanol. After drying with a nitrogen flow, 80  $\mu\text{l}$  of dense colloidal ink was loaded on a silicon wafer positioned in the enclosed chamber by drop-casting and maintained for 7 hours. The evaporative self-assembled thin-film of the nanoparticles was then annealed at 500 °C for 1 hour, inducing thermal degradation of PVP and sintering metal domains.<sup>4</sup>

**Measurement of Bulk Complex Refractive Index.** Macroscopic optical functions of Au and  $\text{Au}_{1-x}\text{Cu}_x$  series were obtained using spectroscopic ellipsometry (SE), which measures phase shift ( $\Delta$ ) and light amplitude ratio ( $\Psi$ ) from elliptically polarized light, simultaneously. The ratio ( $\rho$ ) of the p-polarized and s-polarized complex Fresnel reflection coefficients (parallel and perpendicular to the plane of incidence) is expressed in terms of the two angles  $\Psi$  and  $\Delta$ , as follows:

$$\rho(\lambda, d, N_0, N_1, N_2) = \frac{r(p)}{r(s)} = \tan \Psi e^{i\Delta}$$

$$\langle \varepsilon \rangle = \langle \varepsilon_1 \rangle + i\langle \varepsilon_2 \rangle = \langle \tilde{n} \rangle^2 = (\langle n \rangle + i\langle k \rangle)^2 = \sin(\phi)^2 \cdot \left[ 1 + \tan(\phi)^2 \cdot \left( \frac{1 - \rho}{1 + \rho} \right)^2 \right]$$

Experimental data were measured in the range of 450 to 1000 nm with a beam spot size of 0.3 mm. D2 lamp and Xe lamp (75 W) were used as a light source, and beam incident angle

changed from 45° to 90°. Fitting of experimental data was conducted using cubic B-spline function to obtain the complex refractive index of Au and intermetallic  $\text{Au}_{1-x}\text{Cu}_x$  series.<sup>5</sup>

## 2. Supplementary Figures

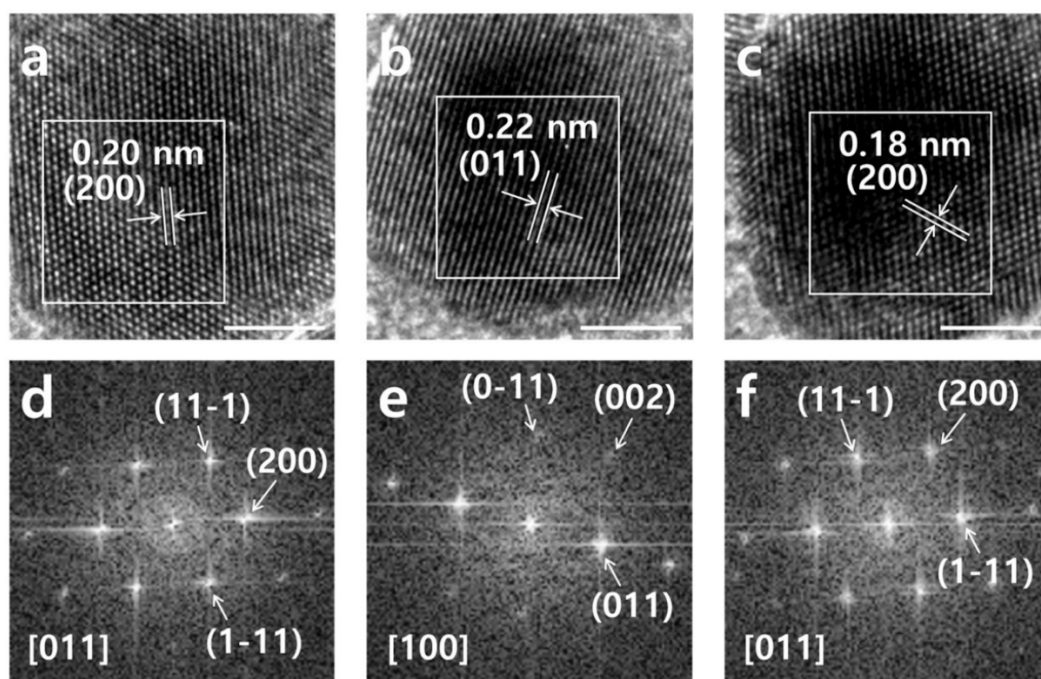


**Figure S1.** HRTEM and fast Fourier transform (FFT) pattern images of (a,d)  $\text{Au}_3\text{Cu}$ , (b,e)  $\text{AuCu}$ , and (c,f)  $\text{AuCu}_3$ . The scale bars represent 5 nm. The FFT patterns were obtained from the white square region and the square brackets indicate the zone axis.

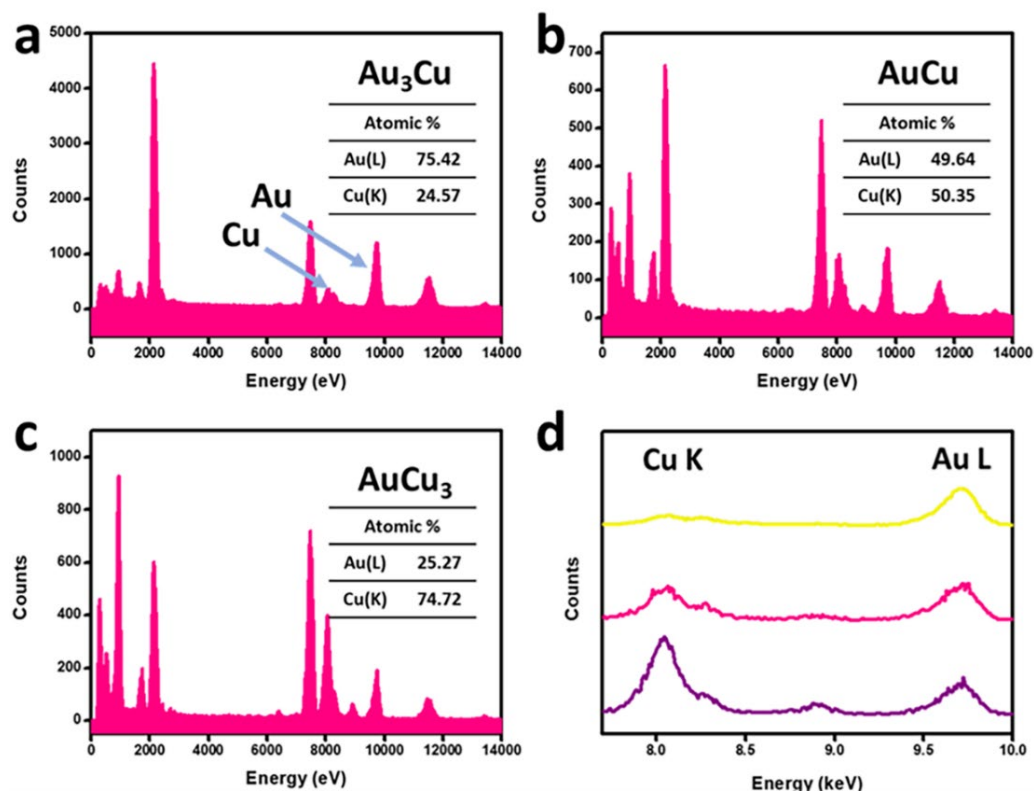


**Figure S2.** (a,b,c) EDS data of intermetallic  $\text{Au}_{1-x}\text{Cu}_x$  nanoparticles. (d) Compositional changes of Cu K and Au L in the range of 7.5 to 10 keV.

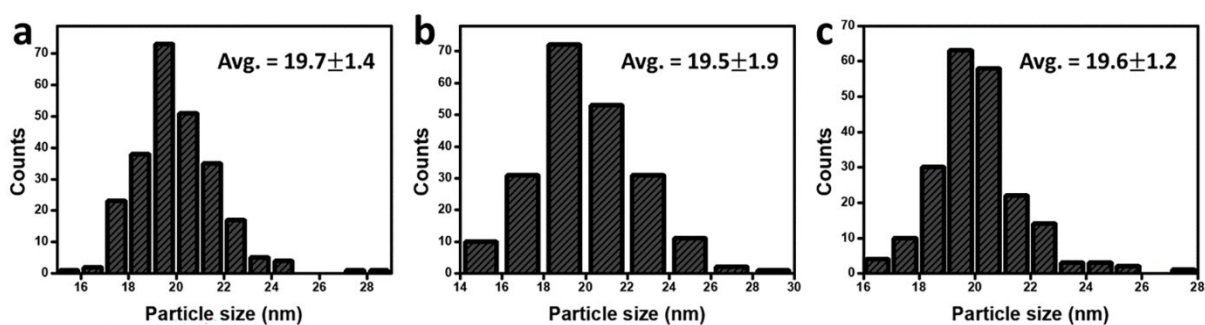


**Figure S3.** Size-distribution histogram of intermetallic (a)  $\text{Au}_3\text{Cu}$ , (b)  $\text{AuCu}$ , and (c)  $\text{AuCu}_3$  nanoparticles.

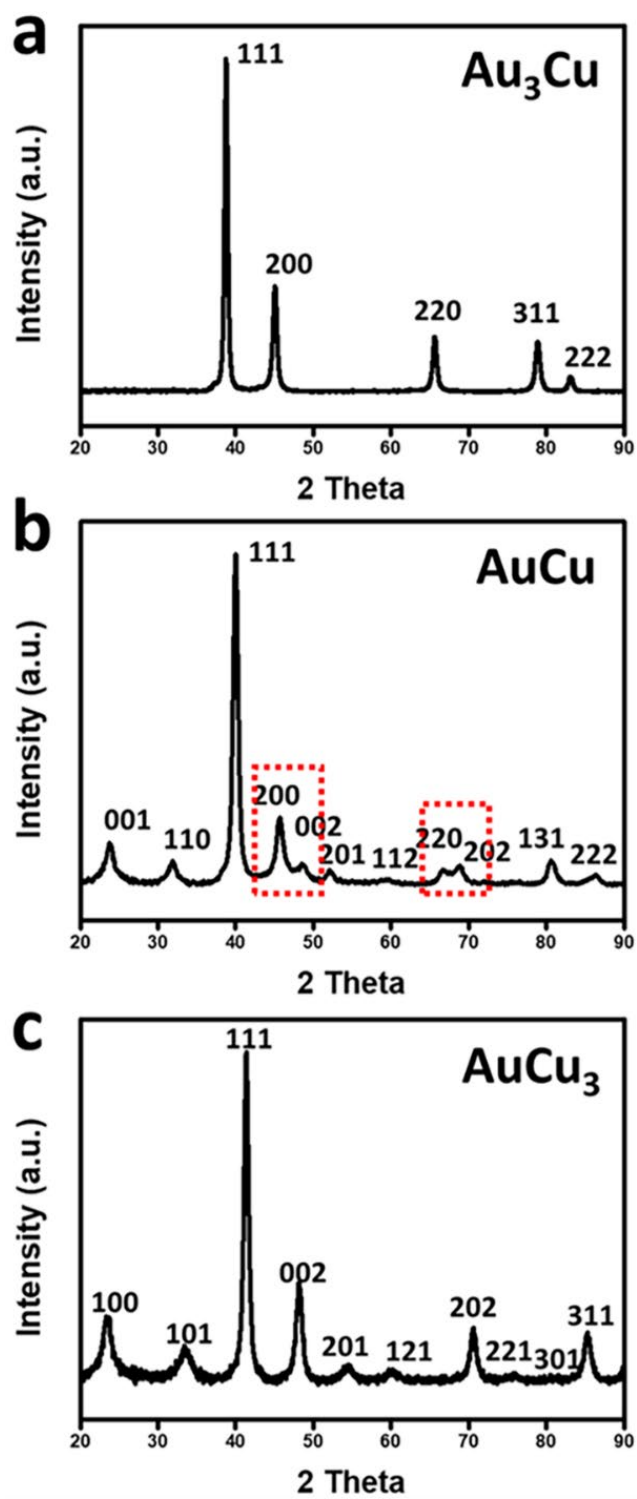


**Figure S4.** The XRD data of intermetallic (a) Au<sub>3</sub>Cu, (b) AuCu, and (c) AuCu<sub>3</sub> nanoparticles.

**Estimation of the Long-Range Order Parameter.** The long-range order parameter (S), which indicates the deviation from perfect order, is defined as:

$$S = \frac{r_A - F_A}{1 - F_A}$$

where  $r_A$ = fraction of A sites occupied by the “right” atoms, and  $F_A$ = fraction of A atoms in the alloy. Parameter S could be determined experimentally by comparing the integrated intensity ratio of a superlattice and a fundamental line.

$$I \propto S^2 |F|^2 \cdot M \cdot LP$$

$$\frac{\text{Intensity (superlattice line)}}{\text{Intensity (fundamental line)}} = \frac{S^2 |F|^2 \cdot M \cdot LP \text{ (superlattice line)}}{|F|^2 \cdot M \cdot LP \text{ (fundamental line)}}$$

where F is the structure factor, LP is the Lorentz polarization factor, and M is the multiplicity factor. F and LP factors are defined as:

$$F_{hkl} = \sum_i f_i e^{[2\pi i(hx_i + ky_i + lz_i)]}$$

$$LP = \frac{1 + \cos^2 2\theta}{\sin^2 \theta \cos \theta}$$

Here, the calculation of long-range order parameter S was based on the normalized peak intensity ratio of fundamental line and superlattice line with parameters of Table S1. The normalized peak intensity was determined by Gaussian fitting of each peak.<sup>6,7</sup>

**Table S1.** Structure factors, Lorentz polarization factors, and multiplicity factors on fundamental and superlattice diffraction planes of AuCu and AuCu<sub>3</sub> samples.

Peak	Parameters		
	F	LP	M
AuCu (111)	155.16	14.05	8
AuCu (001)	87.42	42.49	2
AuCu <sub>3</sub> (111)	115.15	13.01	8
AuCu <sub>3</sub> (100)	43.84	44.27	6

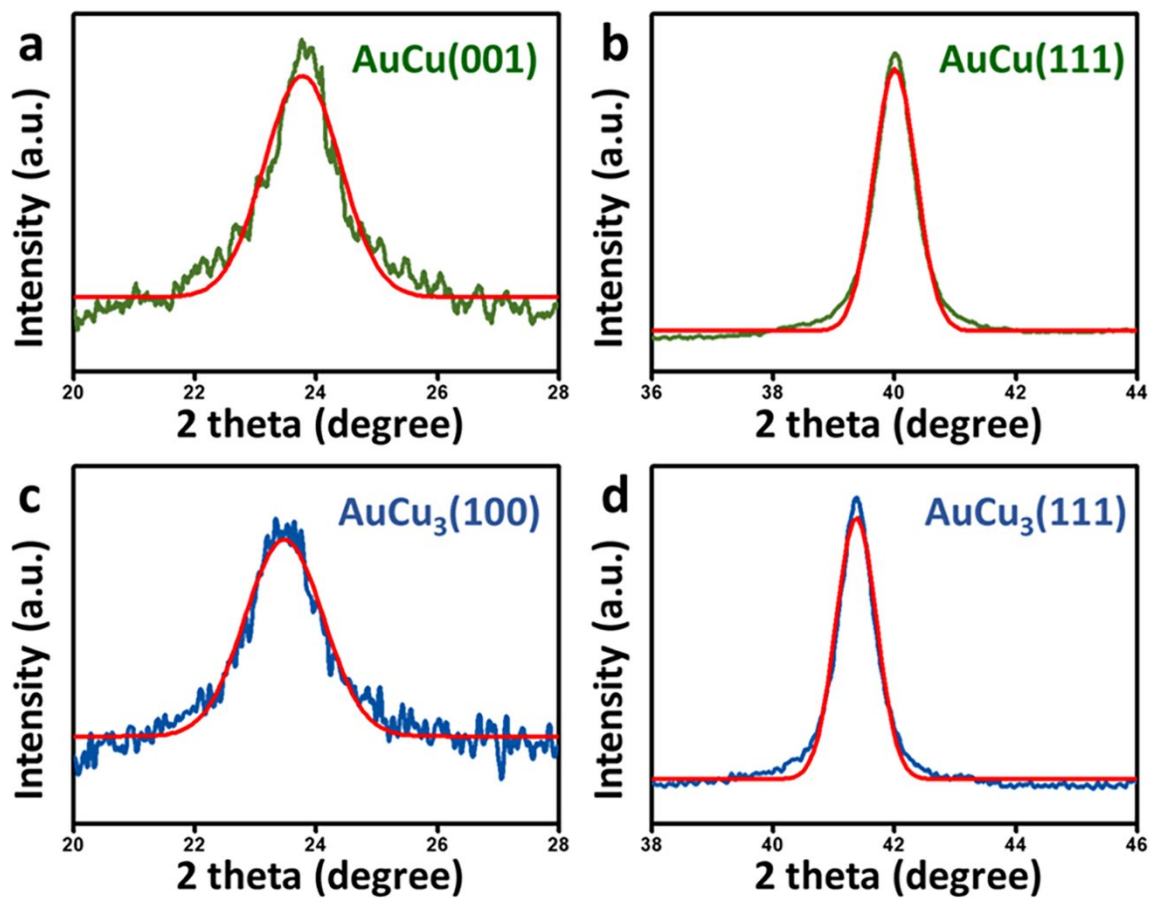


**Figure S5.** Gaussian fitting of (111) and superlattice diffraction peaks of (a,b) AuCu and (c,d) AuCu<sub>3</sub> samples.

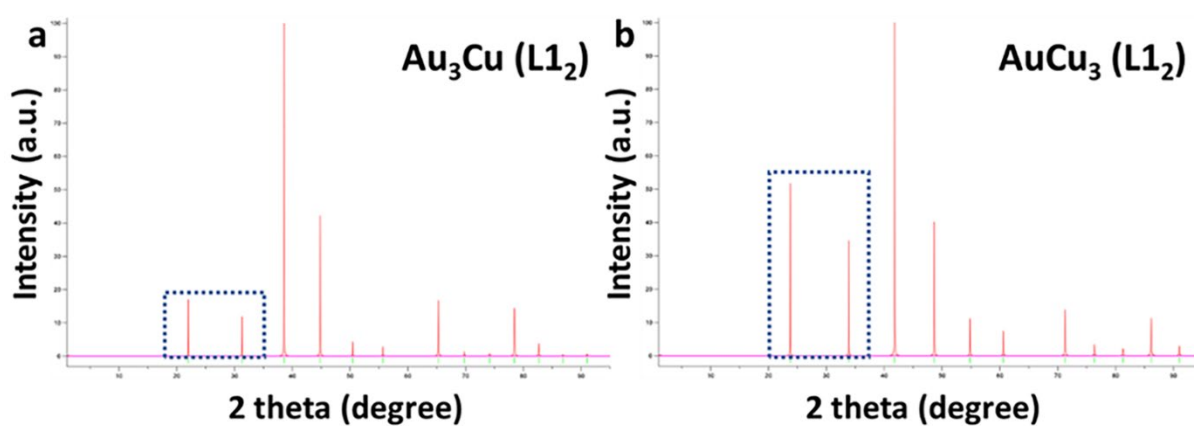


**Figure S6.** Theoretical XRD data of (a) Au<sub>3</sub>Cu and (b) AuCu<sub>3</sub> calculated by VESTA program.



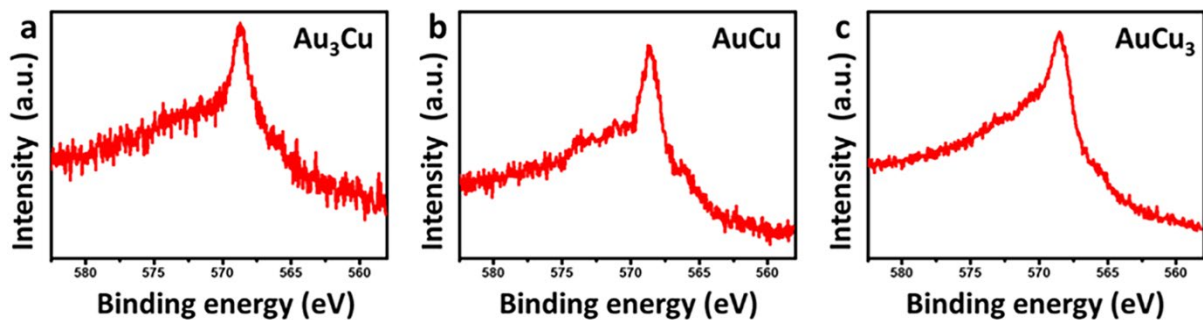


**Figure S7.** Auger spectroscopy data for intermetallic (a)  $\text{Au}_3\text{Cu}$ , (b)  $\text{AuCu}$ , and (c)  $\text{AuCu}_3$  at the Cu LMM region.

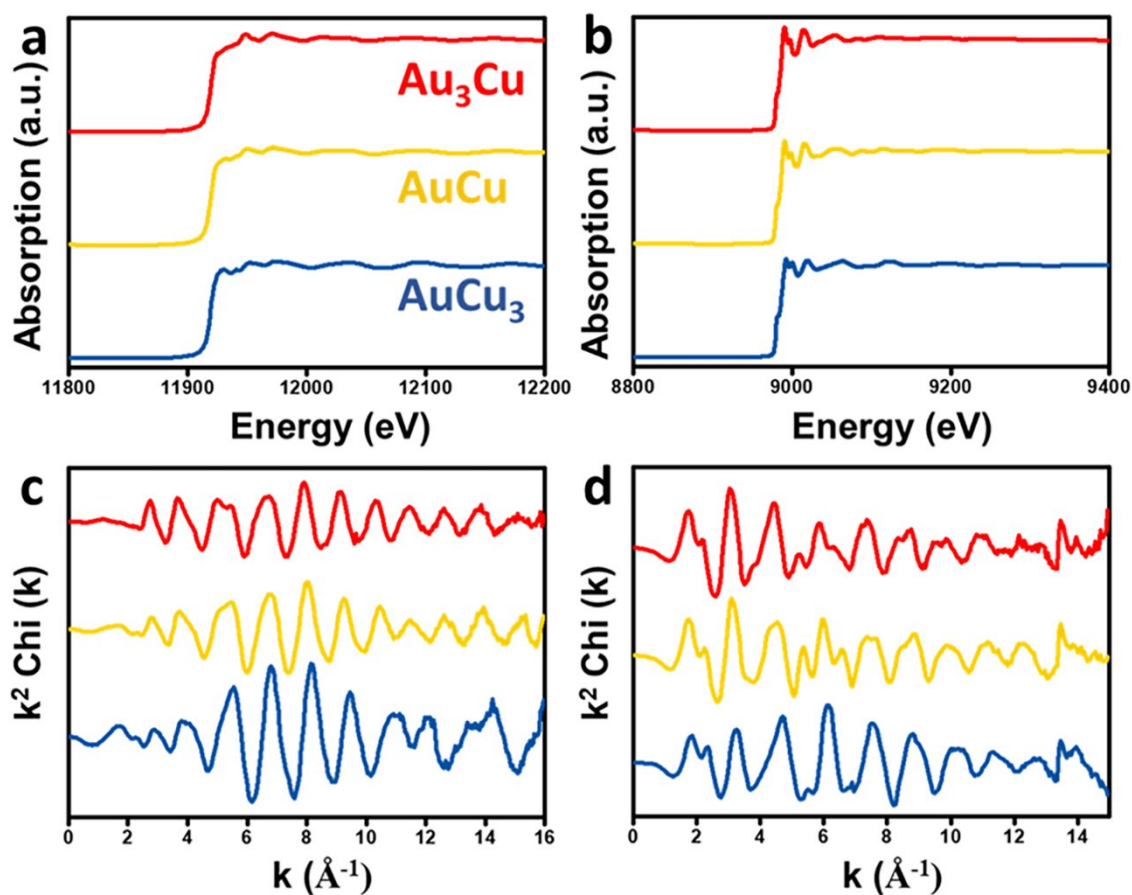


**Figure S8.** (a,b) X-ray absorption and (c,d)  $k^2$ -weight spectra for  $\text{Au}_3\text{Cu}$ ,  $\text{AuCu}$ , and  $\text{AuCu}_3$  at the Au-L<sub>3</sub> edge and Cu K-edge.

**Measurement and Refinement of X-ray Absorption Spectroscopy (XAS) data.** X-ray absorption fine spectroscopy (XAFS) data were collected at Pohang Accelerator Laboratory (7D-XAFS beamline) using Si(111) double crystals as a monochromator where the beam energy and ring current were 2.5 GeV and 300 mA, respectively. The intensity of the incident X-ray radiation ( $I_0$ ) was monitored with a nitrogen-filled ionization chamber. The step and duration time was 0.4 eV and 2.0 s, and the total number of points per XAFS spectrum was 478, sufficient for the analysis of XAFS. The data at the Cu K-edge and Au L<sub>3</sub>-edge were calibrated to a Cu foil and Au foil, respectively. For XAFS analysis, Artemis implemented in the Demeter program package (0.9.25) was utilized after data processing using Athena.<sup>8</sup> Edge step normalization for each spectrum was performed by subtracting the pre-edge and post-edge backgrounds in Athena. The background was removed by fitting data with a cubic spline function, and subsequently, k-space data was Fourier transformed, resulting in an R-space spectrum, which was fit in Artemis using multiple k<sup>2</sup>-weight fitting. Fitting of EXAFS data was performed using the following EXAFS function:

$$\chi(k) = S_0^2 \sum_{i=1}^{N_i} \frac{N_i}{kR_i^2} F_i(K) e^{-2k^2\sigma_i^2} e^{-\frac{2R_i}{\lambda(k)}} \sin[2kR_i - \varphi_i(k)]$$

where the many-body reduction factor ( $S_0^2$ ) was obtained from the curve fit of the XAFS data of reference foil under the same condition and utilized further in the curve fit of the sample. Values for the  $S_0^2$  were determined to be 0.83 for Au and 0.75 for Cu.  $N_i$  and  $R_i$  are the coordination number and half-path length between the central absorbing atom and a scattering atom, respectively. The mean-square disorder ( $\sigma_i$ ) represents thermal fluctuation and structural disorder in the distance from the central absorbing atom to a given shell.<sup>9</sup> These parameters are calculated by fitting the experimental data. The photoelectron mean free path is represented by  $\lambda$ .  $F(k)$  is the backscattering amplitude, and  $\varphi_i(k)$  is the phase factor for a given coordination

shell. The scattering path from the possible model structure was obtained from the *Feff* calculation.

The EXAFS data of the AuCu sample was fit to face-centered tetragonal structure (L1<sub>0</sub>), and to face-centered cubic (L1<sub>2</sub>) for Au<sub>3</sub>Cu and AuCu<sub>3</sub>. The data at the Cu K-edge and Au L<sub>3</sub>-edge were co-fit to represent the actual structure best. The restraints to coordination numbers were applied to describe the intermetallic crystal structures of Au<sub>1-x</sub>Cu<sub>x</sub> series, including  $N_{Au1} = 2 \times N_{Cu1}$  for Au<sub>3</sub>Cu,  $N_{Au1} = \frac{N_{Cu1}}{2}$  and  $N_{Cu1} = 2 \times N_{Au1}$  for AuCu, and  $N_{Cu1} = 2 \times N_{Au1}$  for AuCu<sub>3</sub>.<sup>7</sup>

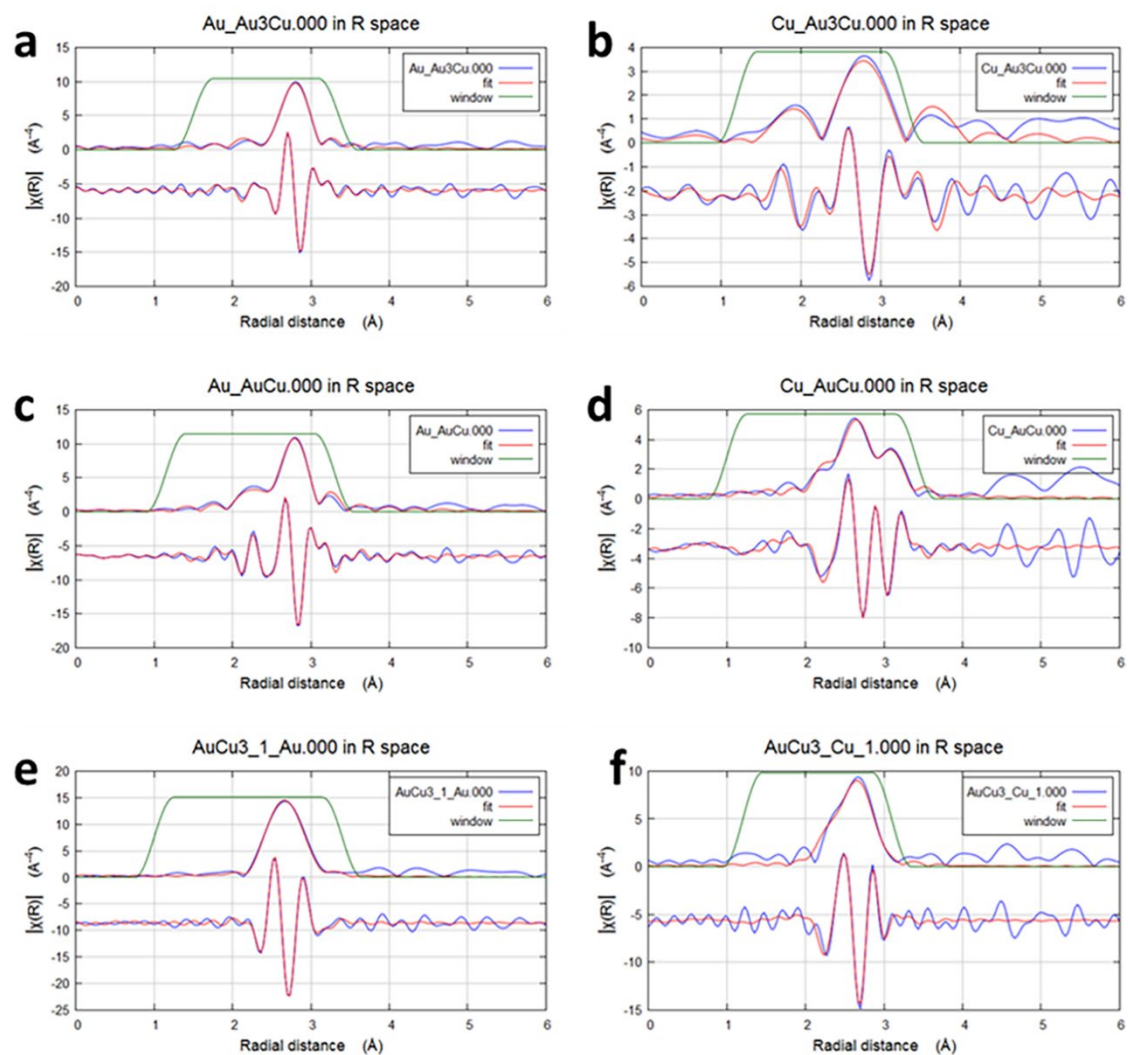


**Figure S9.** The EXAFS refinements in R and q space for (a,b)  $\text{Au}_3\text{Cu}$ , (c,d)  $\text{AuCu}$ , and (e,f)  $\text{AuCu}_3$ .

**Table S2.** Structural parameters around Au L<sub>3</sub>-edge for Au<sub>3</sub>Cu, AuCu, and AuCu<sub>3</sub>.

	Bond	C.N.	R (nm)	$\sigma^2$ (pm <sup>2</sup> )	R-factor
<b>Au<sub>3</sub>Cu</b>	Au-Au	7.65	0.280±0.0003	76±4	0.005
	Au-Cu	3.82±0.44	0.280±0.0013	135±18	
<b>AuCu</b>	Au-Au	3.27±0.38	0.280±0.0006	44±6	0.013
	Au-Cu	6.55	0.269±0.0001	113±13	
<b>AuCu<sub>3</sub></b>	Au-Au				0.013
	Au-Cu	10.34±0.96	0.265±0.0006	86±7	

**Table S3.** Structural parameters around Cu K-edge for Au<sub>3</sub>Cu, AuCu, and AuCu<sub>3</sub>.

	Bond	C.N.	R (nm)	$\sigma^2$ (pm <sup>2</sup> )	R-factor
<b>Au<sub>3</sub>Cu</b>	Cu-Cu				0.019
	Cu-Au	10.16±2.01	0.280±0.002	131±45	
<b>AuCu</b>	Cu-Cu	3.61±0.28	0.280±0.001	198±33	0.016
	Cu-Au	7.22	0.269±0.0008	99±8	
<b>AuCu<sub>3</sub></b>	Cu-Cu	7.26	0.265±0.0008	148±16	0.010
	Cu-Au	3.63±0.32	0.265±0.001	81±15	

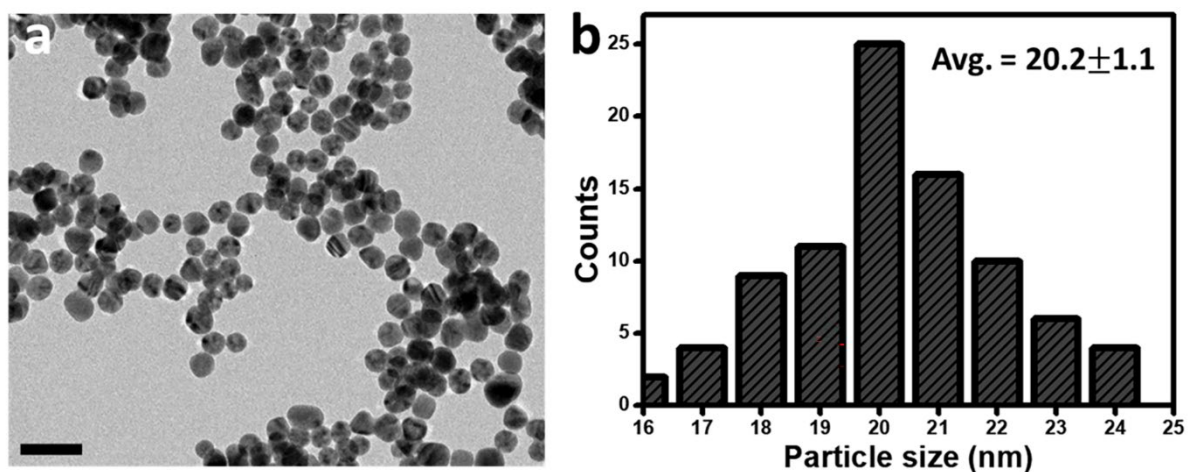


**Figure S10.** (a) TEM image and (b) size-distribution histogram of Au nanoparticles prepared by seed-mediated growth and ligand exchange with PVP. The scale bar represents 50 nm.

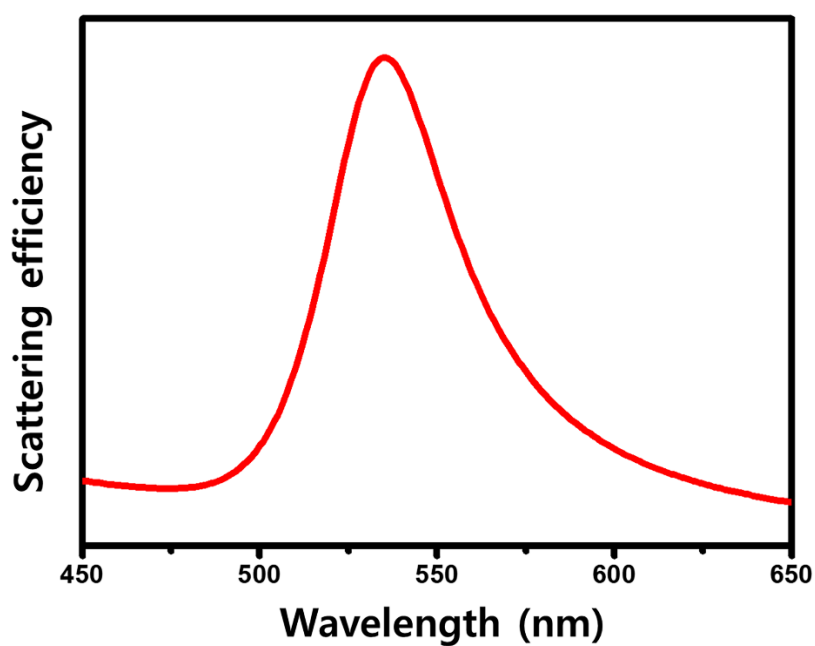


**Figure S11.** Plasmon scattering efficiency of Au nanosphere with a diameter of 20 nm by Mie calculation.<sup>3</sup>

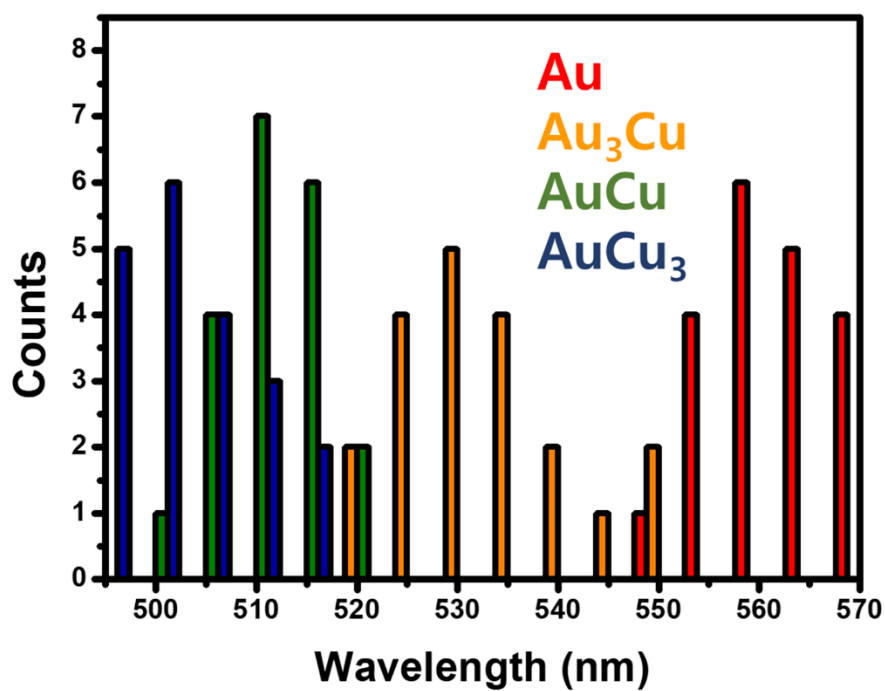


**Figure S12.** Peak maximum-dispersion histogram of single-particle plasmon light scattering spectra for Au, Au<sub>3</sub>Cu, AuCu, and AuCu<sub>3</sub>.

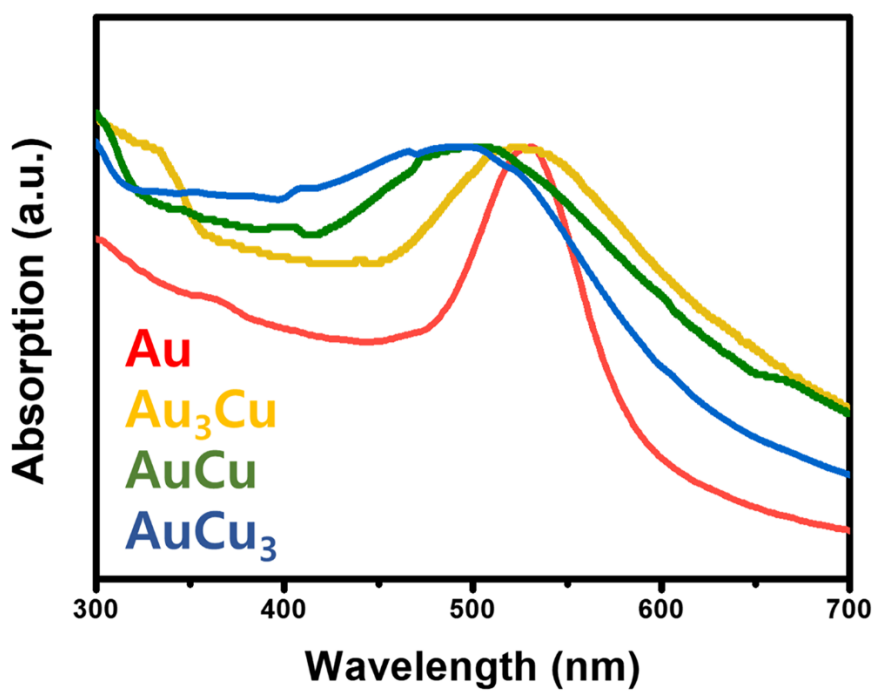


**Figure S13.** Normalized UV-visible absorption spectra of Au, Au<sub>3</sub>Cu, AuCu, and AuCu<sub>3</sub> nanoparticles in aqueous media.

## Bulk experiment

### (1) Evaporation-induced self-assembly

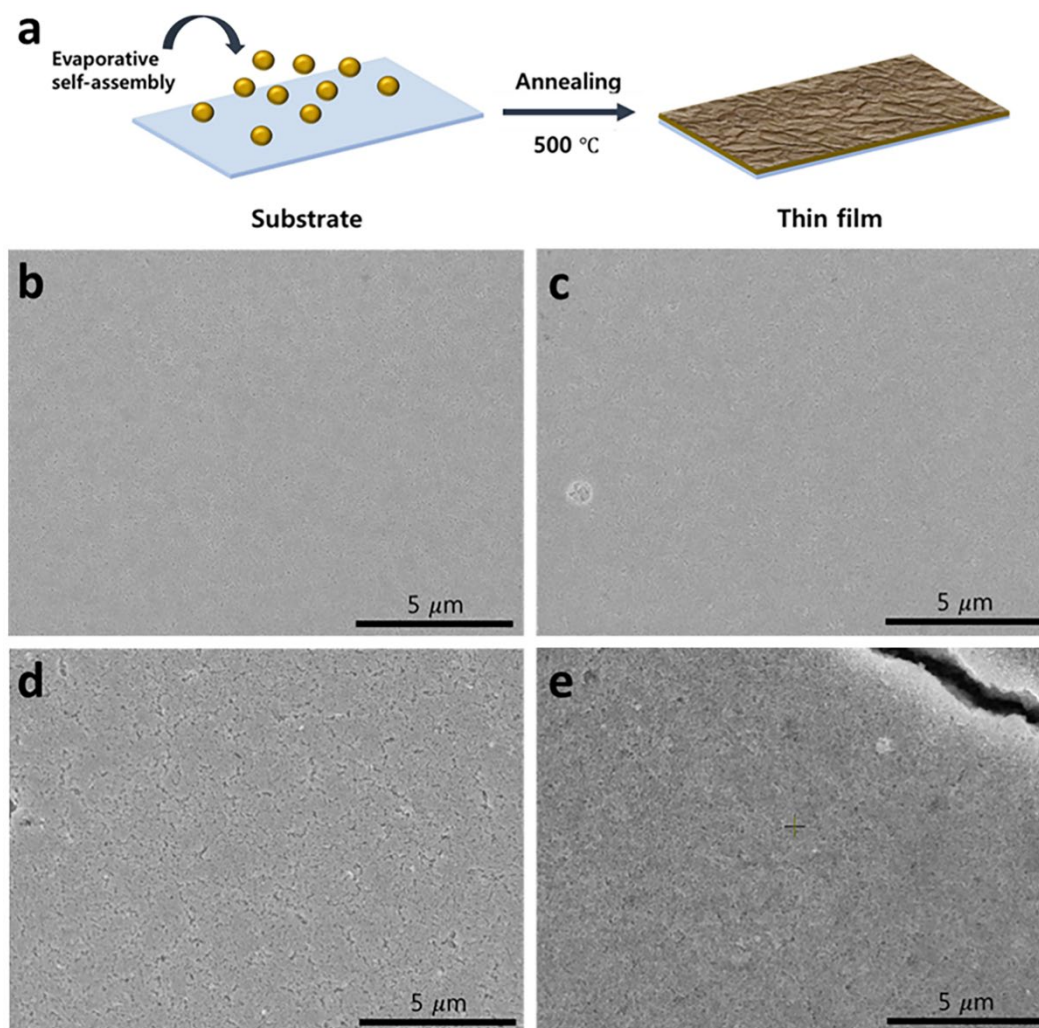


**Figure S14.** (a) Schematic illustration of thin-film fabrication using the evaporation-induced self-assembly and heat treatment. (b,c,d,e) SEM images of the thin-film with Au, Au<sub>3</sub>Cu, AuCu, and AuCu<sub>3</sub> nanoparticles, respectively.

We conducted bulk experiments to demonstrate the abnormal blue-shift in plasmonics of intermetallic Au<sub>1-x</sub>Cu<sub>x</sub> nanoparticles by fabricating self-assembled thin-films.<sup>10</sup> The intrinsic photophysical properties can be considered complex permittivities obtained by mathematically



transforming the complex refractive index of the films measured by SE techniques. We optimized the colloid concentration and evaporation rate of the solvent for the uniform evaporative self-assembly throughout the  $10 \times 10 \text{ mm}^2$  sample region. The resulting thin-films of Au and intermetallic series showed the well-controlled surface conditions over the entire region, circumventing diffuse reflection, which can induce the incorrect interpretation of spectroscopic data. The uniformity in particle size reduced both poly-disperse aggregates and surface roughness by size-dependent van der Waals interactions. Besides, considering the thermodynamic aspects of the particle density of colloids, closed packed superstructures of solid phase are thermodynamically favored with the greater free volume at relatively high density.<sup>11,12</sup> Our experiments were conducted with the high density of colloidal ink under the optimal conditions. Considering the kinetic aspect, the longer the evaporation time, the more the rearrangement time of the particles is ensured. The uniform self-assembly can be achieved from the surface of the colloidal droplet at the intermediate step.<sup>13</sup> We used a closed chamber and ethanol as a solvent to control the evaporation kinetics. Solvents with higher viscosity help to increase the evaporation time but provide the chance of concentric rings characteristic due to mass, thermal, and surface tension gradients.<sup>14-16</sup>

## (2) Characterization

After annealing, the XRD data showed the crystal structures for  $\text{Au}_3\text{Cu}$  ( $\text{L1}_2$ ),  $\text{AuCu}$  ( $\text{L1}_0$ ), and  $\text{AuCu}_3$  ( $\text{L1}_2$ ) (Figure S15a,b,c). However, a partial disordering in the  $\text{AuCu}$  sample is observed by thermal disintegration of intermetallic arrangements, resulting in decreased superlattice peaks. The harsher conditions than our optimal ones give rise to the atomic disordering and large porosity from the sintering of nanoparticles. The formed voids can

change the distribution of electron density and electronic band structure, changing the complex refractive index.<sup>17,18</sup>

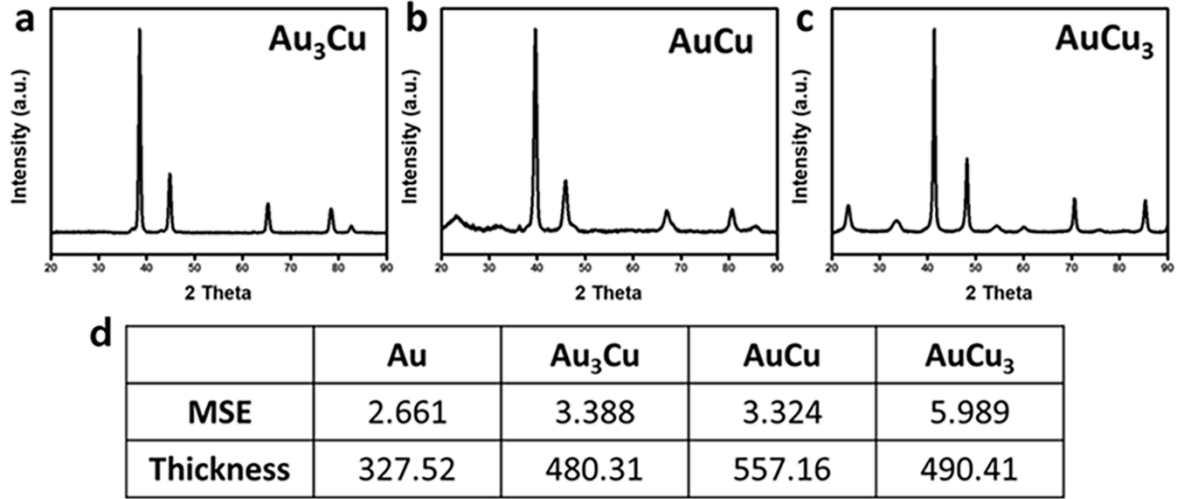


**Figure S15.** (a,b,c) The XRD data after heat treatment. (d) Mean squared error and thickness of Au and intermetallic  $\text{Au}_{1-x}\text{Cu}_x$  samples measured using SE techniques.

We obtained the mean squared error (MSE) for evaluation of fit quality, which quantifies the difference between the model and experiment for all regressed quantities. The random measurement error for each data point was incorporated via the following Levenberg-Marquardt algorithm:

$$\text{MSE} = \frac{1}{2N - M} \sum_{i=1}^N \left[ \left( \frac{\Psi_i^{\text{mod}} - \Psi_i^{\text{exp}}}{\sigma_{\Psi,i}^{\text{exp}}} \right)^2 + \left( \frac{\Delta_i^{\text{mod}} - \Delta_i^{\text{exp}}}{\sigma_{\Delta,i}^{\text{exp}}} \right)^2 \right]$$

where  $N$  is the number of measured  $\Psi$  and  $\Delta$  pairs,  $M$  is the total number of real-valued fit parameters, and  $\sigma_{\Psi,i}^{\text{exp}}$  and  $\sigma_{\Delta,i}^{\text{exp}}$  are the standard deviations of  $\Psi$  and  $\Delta$ . The standard deviations are measured using multiple revolutions of the analyzer (multiple revolutions are used in any case to improve the signal-to-noise ratio for  $\Psi$  and  $\Delta$ ).<sup>5</sup> The goal of the data analysis is to

minimize the MSE by adjusting the unknown parameters for the various layers. In this way, unknown parameters in the model, as optical constants and thickness of layers, can be fitted and extracted from measured SE data. By fitting the experimental results using the B-spline function, The MSE is highly reliable when the square root of this value is less than 4.<sup>19</sup>

### (3) Plasmon light scattering efficiency

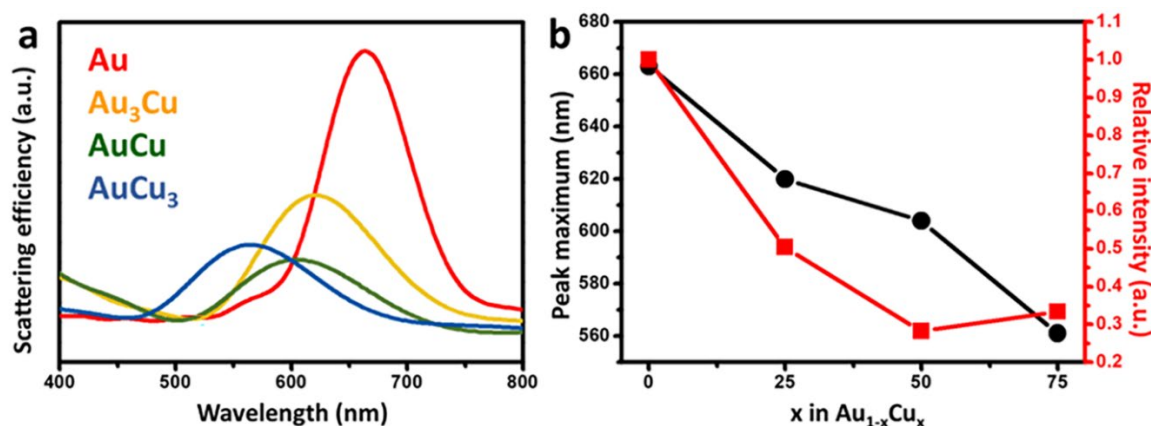


**Figure S16.** (a) Theoretical plasmon scattering efficiencies using the measured complex permittivities. (b) Scattering peak maxima and relative intensities as a function of composition.

Voids, surface roughness, and partial disordering by annealing probably caused differences between measured bulk permittivity values and the complex permittivity of the initial nanoparticles.<sup>17,18</sup> In the region of plasmon resonance, the measured optical functions showed similar features with calculated structures, but the closer to the IR region of a much longer wavelength, the larger the values than expected. For comparison with the single-particle experiment, the plasmon scattering efficiencies are obtained by Mie scattering calculations using measured bulk permittivity values (Figure S16a). The resulting plasmon bands showed the hypsochromic shift of scattering peak maximums with the increasing Cu amounts, as in the single-particle experiments. Changes in scattering peak maximum and intensity were plotted

versus composition (Figure S16b). As the Cu amount increases, it showed a blue shift from 663 to 620, 604, and 561 nm, respectively, showing the overall shift of 102 nm. However, in this bulk experiment, each plasmon resonance was formed in the long-wavelength region due to the grain boundary and the structural porosity caused by the annealing process.<sup>17,18</sup> The plasmon scattering intensities are decreased with the increasing Cu content and almost saturated in AuCu<sub>3</sub>.

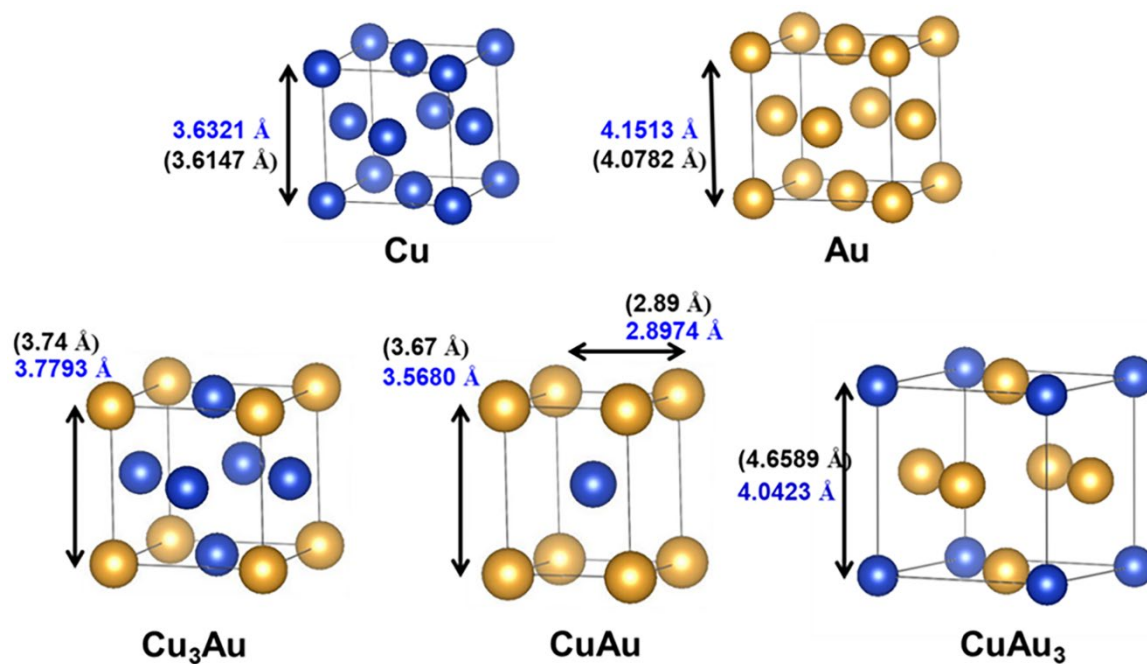


**Figure S17.** The optimized cell parameters for pure metals and intermetallic  $\text{Au}_{1-x}\text{Cu}_x$  series to calculate the complex permittivities. Numbers in parentheses indicate reference values (Au, JCPDS 03-065-2870;  $\text{Au}_3\text{Cu}$ , JCPDS 01-071-5023;  $\text{AuCu}$ , JCPDS 00-025-1220;  $\text{AuCu}_3$ , JCPDS 03-065-3249; Cu, JCPDS 00-004-0836).

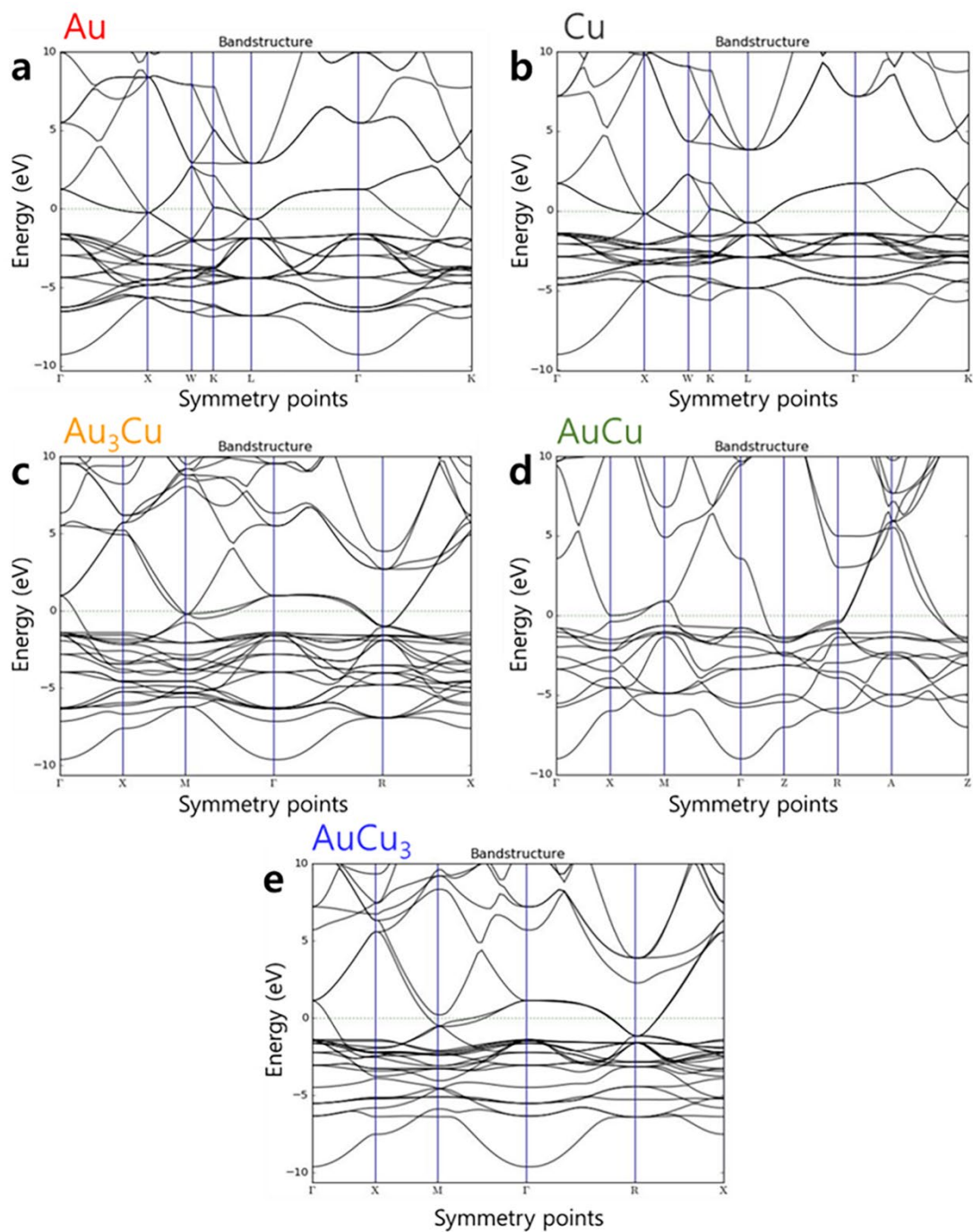


**Figure S18.** Electronic band structures for Au, Cu, Au<sub>3</sub>Cu, AuCu, and AuCu<sub>3</sub> by density functional calculations.

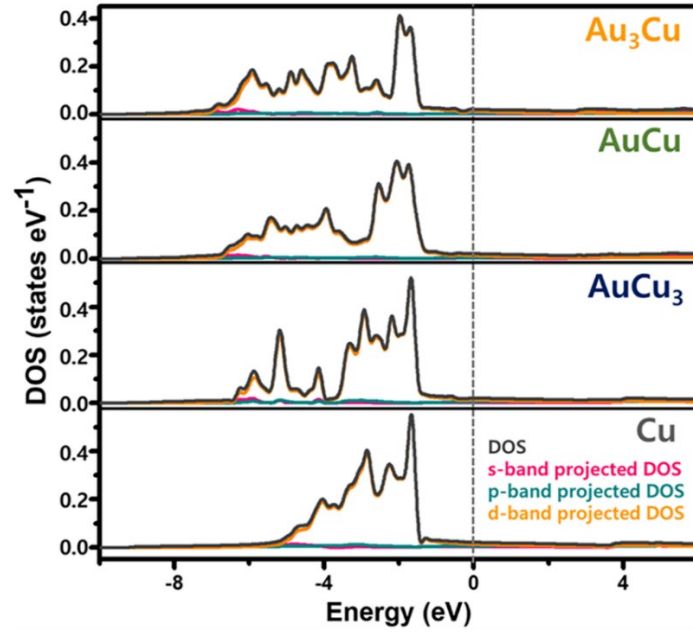


**Figure S19.** The density of states for  $\text{Au}_3\text{Cu}$ ,  $\text{AuCu}$ ,  $\text{AuCu}_3$ , and  $\text{Cu}$  with the projected DOS.

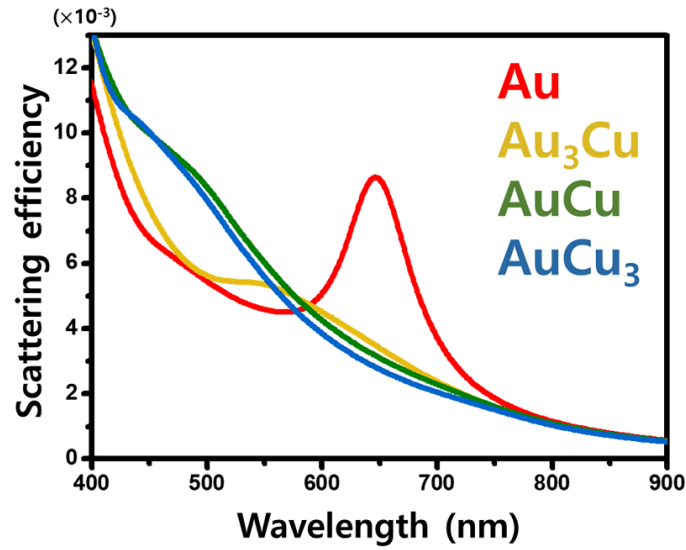


**Figure S20.** Plasmon scattering efficiencies of  $\text{Au}$ ,  $\text{Au}_3\text{Cu}$ ,  $\text{AuCu}$ , and  $\text{AuCu}_3$  spheres with a diameter of 20 nm by Mie calculations. The subtraction of the  $1/\lambda^4$ -background signals leads to **Figure 5(a)**. The background signals were obtained with permittivity values at a fixed 2,066-nm wavelength. No serious dependence of the resulting spectra on the permittivity values selected for generation of the background spectra was found, as long as they were chosen at a wavelength of near 2,000 nm or longer.

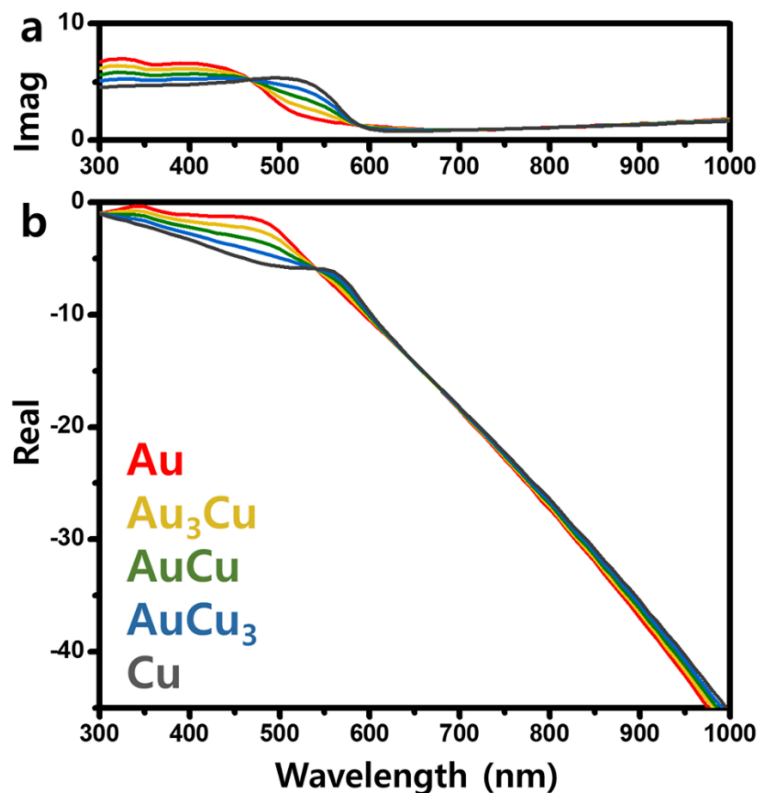


**Figure S21.** (a) Imaginary and (b) real parts of complex permittivities of intermetallic  $\text{Au}_{1-x}\text{Cu}_x$  series using the weighted sum of permittivity values of Au and Cu.<sup>3</sup>

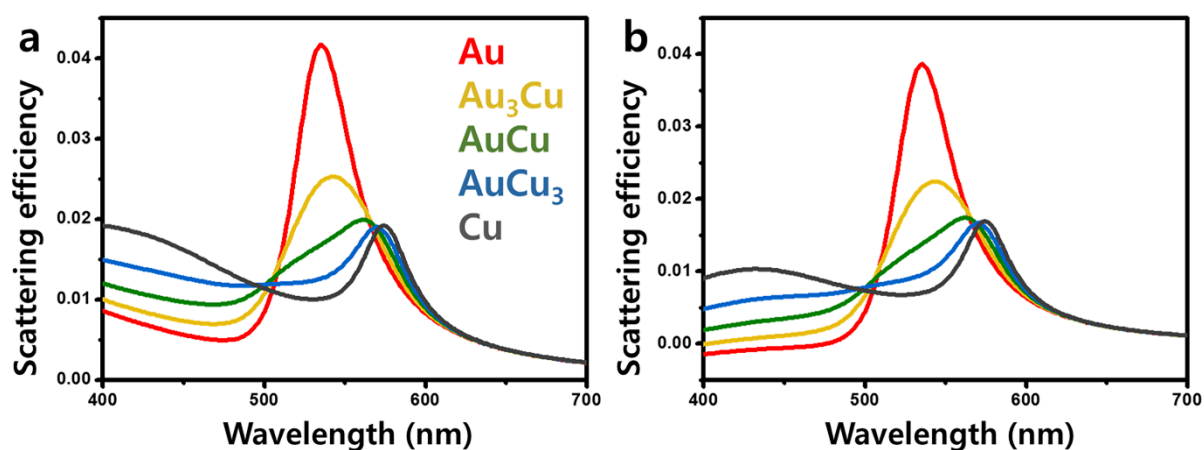


**Figure S22.** (a) Mie scattering and (b) corresponding  $1/\lambda^4$ -background-free signals of Au, Cu, and  $\text{Au}_{1-x}\text{Cu}_x$  spheres using a linear-combination model. In (b), the background signals in (a) were subtracted using the permittivity values at the longest available wavelength of 1,700 nm.<sup>3</sup>



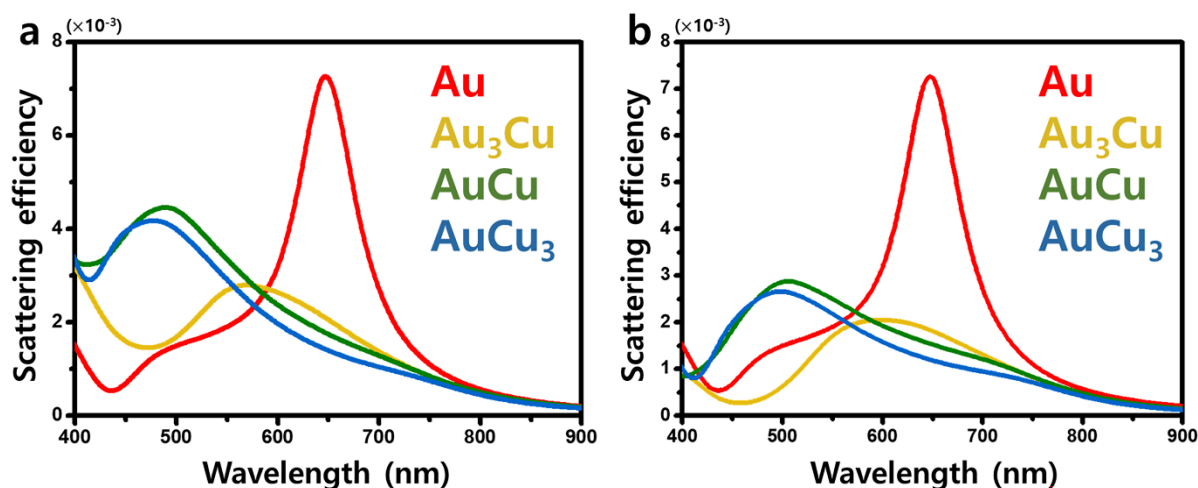


**Figure S23.** Background-free Mie scattering signals for Au and intermetallic  $\text{Au}_{1-x}\text{Cu}_x$  spheres (a) without and (b) with a CuO layer of 0.5 nm.<sup>20</sup> The intermetallic  $\text{Au}_{1-x}\text{Cu}_x$  nanoparticles of a 20 nm diameter with a CuO semiconductor layer of 0.5 nm showed the intensity attenuation of 26 % for  $\text{Au}_3\text{Cu}$  and 36 % for  $\text{AuCu}$  and  $\text{AuCu}_3$ , respectively, compared to no oxide shell cases. The scattering peak maxima are generated at 590, 505, 496 nm for  $\text{Au}_3\text{Cu}$ ,  $\text{AuCu}$ , and  $\text{AuCu}_3$ , respectively, which were red-shifted by about 10 nm, still showing distinctive hypsochromic shifts.

### 3. References

1. Piella, J.; Bastús, N. G.; Puentes, V. Size-Controlled Synthesis of Sub-10-Nanometer Citrate-Stabilized Gold Nanoparticles and Related Optical Properties. *Chem. Mater.* **2016**, *28*, 1066-1075.
2. Rostek, A.; Mahl, D.; Epple, M. Chemical Composition of Surface-Functionalized Gold Nanoparticles. *J. Nanopart. Res.* **2011**, *13*, 4809-4814.
3. McPeak, K. M.; Jayanti, S. V.; Kress, S. J. P.; Meyer, S.; Iotti, S.; Rossinelli, A.; Norris, D. J. Plasmonic Films Can Easily Be Better: Rules and Recipes. *ACS Photonics* **2015**, *2*, 326-333.

4. Loría-Bastarrachea, M. I.; Herrera-Kao, W.; Cauich-Rodriguez, J. V.; Cervantes-Uc, J. M.; Vázquez-Torres, H.; Ávila-Ortega, A. A TG/FTIR Study on the Thermal Degradation of Poly(vinyl pyrrolidone). *J. Therm. Anal. Calorim.* **2011**, *104*, 737-742.
5. Jellison Jr, G. E. Data Analysis for Spectroscopic Ellipsometry. *Thin Solid Films* **1993**, *234*, 416-422.
6. Cullity, B. D.; Stock, S. R. Elements of X-Ray Diffraction, 3<sup>rd</sup> ed.; Pearson: London, **2001**.
7. Kim, D.; Xie, C.; Becknell, N.; Yu, Y.; Karamad, M.; Chan, K.; Crumlin, E. J.; Nørskov, J. K.; Yang, P. Electrochemical Activation of CO<sub>2</sub> through Atomic Ordering Transformations of AuCu Nanoparticles. *J. Am. Chem. Soc.* **2017**, *139*, 8329-8336.
8. Ravel, B.; Newville, M. ATHENA, ARTEMIS, HEPHAESTUS: Data Analysis for X-ray Absorption Spectroscopy Using IFEFFIT. *J. Synchrotron Radiat.* **2005**, *12*, 537-541.
9. Ohta, M.; Nakagawa, M.; Yasuda, K. Initiation of Ordering in an AuCu alloy. *J. Mater. Sci.* **1990**, *25*, 5025-5028.
10. Yang, J.; Choi, M. K.; Kim, D.-H.; Hyeon, T. Designed Assembly and Integration of Colloidal Nanocrystals for Device Applications. *Adv. Mater.* **2016**, *28*, 1176-1207.
11. Frenkel, D. Order through Disorder: Entropy Strikes Back. *Phys. World* **1993**, *6*, 24-25.
12. Acherson, B. J. When Order is Disordered. *Nature* **1993**, *365*, 11-12.
13. Bigioni, T. P.; Lin, X.-M.; Nguyen, T. T.; Corwin, E. I.; Witten, T. A.; Jaeger, H. M. Kinetically Driven Self Assembly of Highly Ordered Nanoparticle Monolayers. *Nat. Mater.* **2006**, *5*, 265-270.

14. Stowell, C.; Korgel, B. A. Self-Assembly Honeycomb Networks of Gold Nanocrystals. *Nano Lett.* **2001**, *11*, 595-600.
15. Ohara, P. C.; Heath, J. R.; Gelbart, W. M. Self-Assembly of Submicrometer Rings of Particles from Solutions of Nanoparticles. *Angew. Chem. Ind. Ed. Engl.* **1997**, *36*, 1077-1080.
16. Deegan, R. D. Pattern Formation in Drying Drops. *Phys. Rev. E* **2000**, *61*, 475-485.
17. De Silva, K. S. B.; Gentle, A.; Arnold, M.; Keast, V. J.; Cortie, M. B. Dielectric Function and Its Predicted Effect on Localized Plasmon Resonances of Equiatomic Au-Cu. *J. Phys. D: Appl. Phys.* **2015**, *48*, 215304.
18. Zhang, H.-L.; Evans, S. D.; Henderson, J. R. Spectroscopic Ellipsometric Evaluation of Gold Nanoparticle Thin Film Fabricated Using Layer-by-Layer Self-Assembly. *Adv. Mater.* **2003**, *15*, 531-534.
19. Gong, C.; Leite, M. S. Noble Metal Alloys for Plasmonics. *ACS Photonics* **2016**, *3*, 507-513.
20. Palik, E. D.; Ghosh, G. *Handbook of Optical Constants of Solids, Volume II*; Academic Press; San Diego, **1998**; pp 875-882.